ACS NANO

www.acsnano.org

ARTICLE

Optically Detected Magnetic Resonance Spectroscopy of Cu-Doped CdSe/CdS and $CuInS_2$ Colloidal Quantum Dots

Adi Harchol,[‖] Yahel Barak,[‖] Kira E. Hughes, Kimberly H. Hartstein, Huygen j. Jöbsis, P. Tim Prins, Celso de Mello Donegá,* Daniel R. Gamelin,* and Efrat Lifshitz*

Cite This: *ACS Nano* 2022, 16, 12866–12877

Read Online

ACCESS | Metrics & More | Article Recommendations | Supporting Information

ABSTRACT: Copper-doped II–VI and copper-based I–III–VI_2 colloidal quantum dots (CQDs) have been at the forefront of interest in nanocrystals over the past decade, attributable to their optically activated copper states. However, the related recombination mechanisms are still unclear. The current work elaborates on recombination processes in such materials by following the spin properties of copper-doped CdSe/CdS (Cu@CdSe/CdS) and of $CuInS_2$ and $CuInS_2$/(CdS, ZnS) core/shell CQDs using continuous-wave and time-resolved optically detected magnetic resonance (ODMR) spectroscopy. The Cu@CdSe/CdS ODMR showed two distinct resonances with different *g* factors and spin relaxation times. The best fit by a spin Hamiltonian simulation suggests that emission comes from recombination of a delocalized electron at the conduction band edge with a hole trapped in a Cu^{2+} site with a weak exchange coupling between the two spins. The ODMR spectra of $CuInS_2$ CQDs (with and without shells) differ significantly from those of the copper-doped II–VI CQDs. They are comprised of a primary resonance accompanied by another resonance at half-field, with a strong correlation between the two, indicating the involvement of a triplet exciton and hence stronger electron–hole exchange coupling than in the doped core/shell CQDs. The spin Hamiltonian simulation shows that the hole is again associated with a photogenerated Cu^{2+} site. The electron resides near this Cu^{2+} site, and its ODMR spectrum shows contributions from superhyperfine coupling to neighboring indium atoms. These observations are consistent with the occurrence of a self-trapped exciton associated with the copper site. The results presented here support models under debate for over a decade and help define the magneto-optical properties of these important materials.

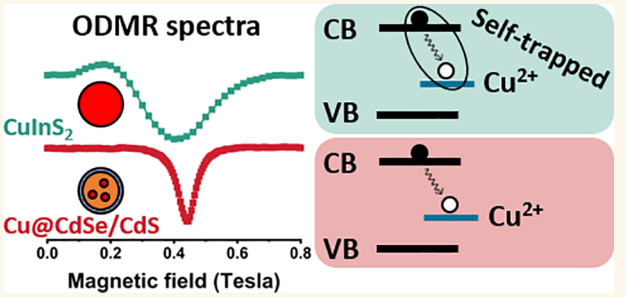

KEYWORDS: *Continuous-Wave Optically Detected Magnetic Resonance, Colloidal Quantum Dots, Semiconductors, Photoluminescence, Copper-Doped, Core/Shell*

The incorporation and characterization of metal ion impurities in colloidal quantum dots (CQDs) have garnered broad scientific and technological interest during the past decade.[1−3] Copper-doped II–VI and copper-based I–III–VI_2 CQDs are of particular interest, attributable to their photophysical properties such as optically activated copper states, band-edge tunability, a significant emission Stokes shift with a lack of reabsorption, an extended lifetime, and toxic-element-free (in I–III–VI_2) composition.[4−6] These copper-mediated properties underpin the utility of these materials in photovoltaic cells,[7] luminescent solar concentrators,[8−10] low-threshold lasers,[11] water splitting,[12] and bioimaging.[13]

Copper impurities in bulk II–VI and III–V semiconductors were extensively studied at the end of the previous century. Those binary semiconductors possess zinc-blende or wurtzite crystal structures, in which their electronic structure is dominated by a heavy hole at the valence band edge (ligand p orbital) and a light electron (metal s orbital) at the conduction band edge. Copper ions in II–VI semiconductors experience a tetrahedral crystal field, which splits their d orbitals into a lower-lying e pair and an upper t_2 triply degenerate set. It was proposed that photoexcitation of Cu^+ and Al^{3+}/Cl^--doped ZnS formally oxidizes Cu^+ sites to form a

Received: May 25, 2022
Accepted: July 27, 2022
Published: August 1, 2022

metastable Cu^{2+} deep acceptor in its $^2T_2$ state, while the Al^{3+} or Cl^- sites bind the photogenerated electrons and behave as metastable shallow donors.[14,15] Donor−acceptor recombination yields green emission, which has been employed in display technologies.[16] A study of Cu^{2+}-doped CdS bulk crystals revealed sharp and structured emission in the near-IR region attributable to the $^2T_2 \leftrightarrow {}^2E$ d−d transition.[17] Cu-doped GaP bulk crystals possessed recombination between Cu^{2+} at a substitutional Ga site ($Cu^{2+}_{(Ga)}$) and Cu^+ at an interstitial site ($Cu^+_{(i)}$), together acting as a donor−acceptor pair.[18] The emission process in the Cu-doped bulk ZnSe crystal was associated with a $Cu_{(Zn)}$ and $Cu_{(Se)}$ donor−acceptor recombination in the green spectral region, and the transformation $Cu^{2+} \rightarrow Cu^+$ has been shown to result in near-infrared emission.[19]

The benchmark bulk copper-based semiconductor $CuInS_2$ attracted considerable interest in the previous century as a potential component in solar cells.[20,21] The electronic structure of this compound differs from those of the binary semiconductors because its valence band edge is composed of hybridized Cu(d) and S(p) orbitals, and their conduction band edge has an In(5s) character.[22,23] Whereas the absorption reflects the band gap transitions, optical studies of bulk $CuInS_2$ showed that the photoluminescence (PL) involves intragap recombination processes associated with a variety of defects, such as Cu_{In}, In_{Cu}, V_S, V_{In}, V_{Cu}, and $Cu_{(i)}$.[24,25]

A plethora of investigations arose with the development of copper-doped II−VI and III−V and copper-based I−III−VI_2 CQDs.[4,6,26] Several studies on Cu-doped II−VI CQDs proposed a mechanism in which a conduction-band electron recombines with a midgap trapped hole on a copper site.[27,28] Such a band to acceptor recombination resembles the luminescence of metal to ligand charge-transfer excited states in Cu^+ molecular compounds, with a typically deep and broad emission and a long lifetime, and is thus sometimes referred to as a metal-to-ligand (conduction band) charge transfer ($ML_{(CB)}CT$) process.[4] The extended lifetime is related to the localized character of the deeply trapped Cu(d)-based hole. Despite the consensus about the band to acceptor recombination mechanism, there is considerable ambiguity about other fundamental matters, including the oxidation state of the incorporated dopants in the ground state. Some authors suggest the integration of diamagnetic Cu^+ ($[Ar]3d^{10}$) dopants in doped II−VI CQDs,[14,29] while others propose the incorporation of paramagnetic Cu^{2+} ($[Ar]3d^9$) ions.[5,30] Multiple interpretations are also given for the large full-width at half-maximum of the midgap emission band, involving a large inhomogeneous broadening,[5,31] transitions to two different energy states of the Cu^{2+} deep acceptor (T_2 and E),[29] or strong vibronic coupling associated with nuclear reorganization at the dopant in the $ML_{(CB)}CT$ excited state.[28,32] A magneto-PL investigation by Knowles et al.[28] revealed a singlet−triplet splitting of the band to acceptor transitions, manifested as pronounced circularly polarized emission under an external magnetic field and attributed to an excited-state exchange splitting. Viswanatha et al.[5] investigated Cu-doped inverted ZnSe/CdSe CQDs by magnetic circular dichroism spectroscopy and observed a Zeeman splitting at the absorption edge, proposing the existence of a paramagnetic Cu^{2+} in the ground state. A study of copper doping in GaAs CQDs exposed the formation of midgap states by the dopant, which led to the creation of an n-type character.[33]

Copper-based I−III−VI_2 CQDs also gained considerable interest in the past decade due to their toxic-element-free properties. Those CQDs crystallize as chalcopyrite or wurtzite structures, dictated by the growth conditions,[34−36] and their surface defects vary according to the type of molecular passivation.[34] The chalcopyrite lattice resembles a zinc-blende structure in which the cation sublattice is shared by two species (I and III) in an ordered pattern, albeit resulting in tetragonal distortion.[35] Extensive discussions were developed in recent years about the oxidation state of the copper cation in the $CuInS_2$ CQDs and the related recombination processes.[26] One proposal postulates that all copper-containing CQDs possess similar rare Cu^{2+} defects in their ground state.[37−39] The other proposal suggests that all of these copper-containing CQDs exhibit similar excited-state hole localization at a lattice Cu^+ site that transiently oxidizes it to Cu^{2+} and consequently leads to exciton self-trapping.[28,40]

Effective mass approximation calculations carried out by Shabaev et al.[41] proposed that the deep emission in $CuInS_2$ QDs is associated with a particular band-edge electronic structure, in which the valence band comprises odd and even hole sublevels. Whereas absorption involves an allowed transition from an even level, emission involves the forbidden odd state, thus leading to a deep and broad luminescence. Magneto-optical measurements of Cu-based I−III−VI_2 CQDs by Anand et al.[42] reported size-dependent radiative decay rates and Stokes shifts as well as dark-state emission attributed to enhanced electron−hole spin interaction at low temperature, and these data were interpreted as supporting a free band-edge exciton description of the luminescence. Similar variable-temperature lifetime data in conjunction with variable-temperature magneto-PL data were alternatively interpreted as indicating a singlet−triplet splitting within a self-trapped exciton.[28] Jara et al.[43] exposed the dependence of a recombination mechanism on the Cu−In stoichiometry, showing band-edge recombination emission in Cu-rich cases but deep emission in In-rich CQDs. Fuhr et al.[44] later proposed that the Cu to In ratio is a critical factor in determining intragap states of Cu^+ and Cu^{2+}, readdressing the question of the luminescence mechanism. This study revealed a dual process: one route involves recombination between an electron from the conduction band and an intragap state of Cu^+ when the latter was oxidized while trapping a hole from the valence band. Such a band to trap recombination resembles the $ML_{(CB)}CT$ proposed above for copper-doped II−VI CQDs. A second route involves direct recombination between the conduction-band electron and a pre-existing Cu^{2+} intragap level, with no requirement for an intermediate process of hole trapping. It is essential to mention that both proposed routes still fail to address whether the emission involves optically active Cu-related defects, or instead, whether self-trapping of an exciton takes place when the exciton resides preferentially on Cu lattice sites.[28,40] In any event, the highly localized character of the Cu center bestows a significant Stokes shift and emission band broadening due to phonon coupling.[28] Xia et al.[45] most recently explored the luminescence of single wurtzite $CuInS_2$/ZnS core/shell CQDs in the 4−300 K temperature range. This work uncovered the occurrence of two different events: a band-edge exciton, appearing as a relatively sharp band (in agreement with the assignment given in ref 41), and a second broad emission band at lower energies, emanating from the strong electron−phonon interaction induced by the hole self-trapping, which was reduced with

https://doi.org/10.1021/acsnano.2c05130
ACS Nano 2022, 16, 12866−12877

the addition of the ZnS shell. In contrast, a recent work[46] on the room-temperature PL of single chalcopyrite $CuInS_2$ CQDs with and without CdS shells has reported only broad bands, which were ascribed to radiative recombination of a conduction band electron with a hole localized at Cu^+, thus being subject to strong electron−phonon coupling. Intriguingly, this study demonstrated that the hole localized at the same preferential Cu^+ site after each excitation.[46] Atomistic density functional theory calculations on $CuInS_2$ CQDs described the valence-band edge as Cu(d)-based with large S(p) covalency and a strong propensity for localization that is easily induced by local symmetry breaking: e.g., through electrostatic perturbations by defects, surfaces, or interfaces.[47] Finally, a study of $Ag_{1-x}Cu_xInS_2$ ($0.0 \leq x \leq 1.0$) CQDs showed that their PL converges to that of $CuInS_2$ CQDs already at very small values of x (~0.2), remaining independent of x at larger values of up to 1.0.[48] This result was interpreted as indicating very limited delocalization of photogenerated holes in the luminescent excited states of $CuInS_2$ CQDs. The literature survey above highlights a suite of ambiguities regarding the PL mechanism of both Cu-doped and Cu-based CQDs. To date, this issue was not addressed using optically detected magnetic resonance (ODMR), which facilitates the determination of the surrounding environments of electrons and holes and their g factors and evaluates the associated spin relaxation times,[49] thus enabling an in-depth understanding of the electronic and spin properties of semiconductors and nanomaterials.[50]

Here, we investigate the excited-state electronic structures of luminescent copper-doped and copper-based CQDs using ODMR spectroscopy. Copper-containing CQDs were synthesized by solution-based techniques to form zinc-blende Cu-doped CdSe/CdS and chalcopyrite $CuInS_2$ CQDs with/without ZnS or CdS shells. Then, continuous-wave (CW) and time-resolved ODMR spectroscopy were applied to examine the fundamental magneto-optical properties of these materials. First, we examine the CW-ODMR spectra of the doped and undoped CdSe/CdS core/shell CQDs. Next, we discuss the CW-ODMR spectra of $CuInS_2$ and $CuInS_2$/(CdS, ZnS) CQDs. Finally, we elucidate the PL mechanisms for the copper-doped and copper-based CQDs using spin-Hamiltonian simulations and a spin kinetic model.

RESULTS AND DISCUSSION

Copper-Doped (Cu@CdSe/CdS) and copper-based ($CuInS_2$, $CuInS_2$/(CdS, ZnS)) were prepared and characterized following previously developed procedures.[10,45,46,51] A summary of the structural and stoichiometry properties of the CQDs is provided in the Supporting Information. The core/shell derivatives were mainly used to gain chemical and spectral stability.

Low-temperature (2.5 K) photoluminescence (PL) spectra of CdSe/CdS, Cu@CdSe/CdS, $CuInS_2$, $CuInS_2$/ZnS, and $CuInS_2$/CdS CQDs are shown in Figure 1. The PL spectrum of the CdSe/CdS CQDs comprises an exciton and a deep-defect luminescence band. The spectrum of Cu@CdSe/CdS CQDs shows a single broad band, which is shifted to lower energy in comparison to the undoped CQDs. The spectra of the copper-based CQDs ($CuInS_2$, $CuInS_2$/(CdS, ZnS)) show a similar deep and broad emission band with an energy slightly above that of the Cu@CdSe/CdS CQDs. The room-temperature PL spectra and the corresponding absorption curves of these II−VI and I−III−VI_2 CQDs recorded at 298 K

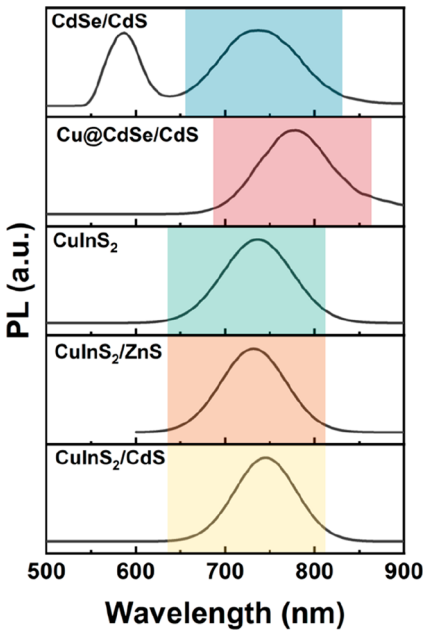

Figure 1. PL curves of CdSe/CdS, Cu@CdSe/CdS, $CuInS_2$, $CuInS_2$/ZnS, and $CuInS_2$/CdS (from top to bottom), acquired at 2.5 K under 405 nm laser excitation. The colored area of the PL emphasizes the spectral window measured by the ODMR method.

are given in Figure S1 in the Supporting Information. The Cu-doped CdSe/CdS CQDs showed typical quantum yield of ~10%.[51] A significant improvement was found in the copper-based CQDs (e.g., 22% for $CuInS_2$ and 86% for $CuInS_2$/CdS).[10,46]

Determining the origin of the deep emission processes was fulfilled by using CW-ODMR spectroscopy. A CW-ODMR spectrum refers to a plot of differential PL intensity ($\Delta I/I$) induced by a magnetic resonance process at the excited state versus the strength of an applied external magnetic field (units of tesla, T).[50] Such a spectrum resembles ground-state ESR but refers to spin-flip events in the emissive excited state; thus, the experiment mainly addresses the spins of the photogenerated carriers. This experiment was performed by placing a sample within a microwave (MW) cavity adapted to the MW frequency of 10.8 GHz. Then, the MW cavity was installed into a magneto-optical cryostat, enabling measurements at low temperatures (2.5 K). The CQDs were irradiated by a continuous-wave laser, with the MW intensity chopped at a variable audio frequency.[52] The chopping frequency also served as a reference for a lock-in detection of the emission intensity under magnetic resonance conditions. Furthermore, the CW-ODMR spectra were recorded both in phase (IP) and out of phase (OP) relative to the MW turn-on time. In addition, the differential PL intensity was monitored either parallel (Faraday configuration) or normal (Voigt configuration) to the direction of the magnetic field.

CW-ODMR Spectra of Undoped and Cu-Doped CdSe/CdS CQDs. Figure 2a,b presents the CW-ODMR spectra of the CdSe/CdS and Cu@CdSe/CdS CQD ensembles, respectively, recorded at 2.5 K and monitored IP (full symbols) and OP (empty symbols) relative to the turn-on time of a MW pulse. These spectra were obtained under a Voigt alignment with 880 Hz MW audio-modulation frequency while the deep PL bands were detected (the colored spectral regions in Figure 1). The CdSe/CdS CQDs IP curve (Figure

https://doi.org/10.1021/acsnano.2c05130
ACS Nano 2022, 16, 12866−12877

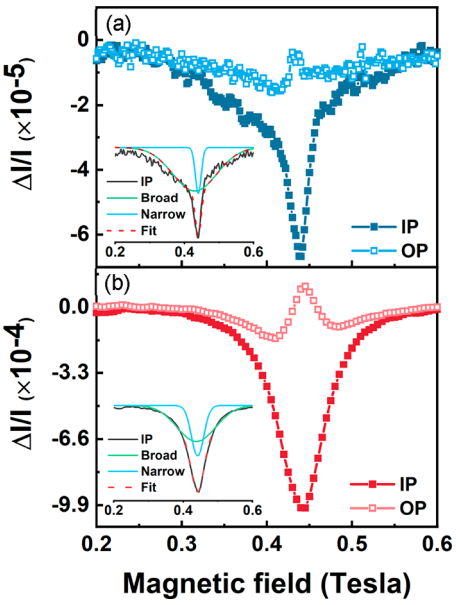

Figure 2. CW-ODMR spectra acquired at 2.5 K under 405 nm laser excitation with a modulation frequency of 880 Hz for (a) CdSe/CdS and (b) Cu@CdSe/CdS CQDs. The insets show the best fit obtained for the IP signal.

2a) shows a negative resonance, which was best fitted by two Gaussians (see the inset) and includes a broad component centered at 0.43 T and a narrow component centered at 0.44 T. The OP curve of CdSe/CdS shows a reduced intensity for the broad component but a drastic sign reversal of the narrow component. The OP measurement corresponds to the recovery of the spins after a spin flip and thus is related to the spin-relaxation time (T_1). Thus, the mentioned components represent two separate carriers with different spin-relaxation times. The signs of the IP and OP ODMR components are dictated by the relative magnitudes of the radiative (τ_R) and spin-relaxation times. A case with $\tau_R < T_1$ leads to an enhancement of the luminescence intensity ($\Delta I/I > 0$, a positive IP signal) due to a spin flip in the excited state. However, when $\tau_R \geq T_1$, the competition between the relaxation processes dictates a thermalization and formation of a negative IP signal, as in the present case, implying the involvement of at least one carrier in a defect site. Therefore, the narrow resonance is identified with a delocalized carrier, such as an electron in a II−VI semiconductor with s orbital character. In contrast, the broad resonance is associated with the spin of a localized hole in an anisotropic environment: e.g., a defect site. Indeed, the relatively intense deep-trap emission of these II−VI CQDs agrees with the existence of interface vacancies generated along a strained core/shell boundary.[53−55] The spin-Hamiltonian simulation elaborated below will further corroborate the resonances' assignment.

The ODMR spectrum of the Cu@CdSe/CdS CQDs, recorded under the same experimental conditions as for the undoped CdSe/CdS CQDs, is presented in Figure 2b. Surprisingly, the IP signal reveals a negative resonance that was also best fitted with two Gaussians (see inset and Figure S2), with trends identical to those seen in the undoped CdSe/CdS CQDs. However, several variations can be identified: the center of the broad resonance experienced a small shift to a

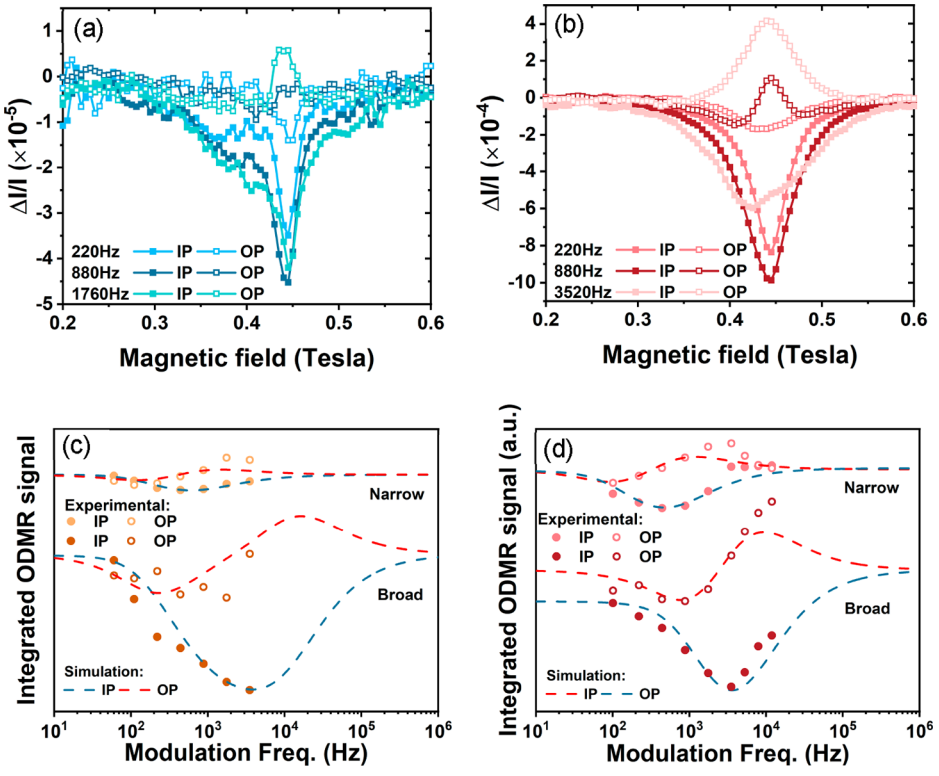

Figure 3. Representative CW-ODMR spectra at different modulation frequencies for (a) CdSe/CdS and (b) Cu@CdSe/CdS CQDs. (c, d) Integrated ODMR signal (IP and OP) for the narrow and broad components as a function of the modulation frequency (log scale) for CdSe/CdS and Cu@CdSe/CdS, respectively. The red and blue dashed lines are fitted simulations to the IP and OP, respectively, according to the kinetic model shown in eq 2. The fit parameters are shown in Table 2 and Table S1.

https://doi.org/10.1021/acsnano.2c05130
ACS Nano 2022, 16, 12866−12877

higher magnetic field (~0.01 T), and the narrow-component width is slightly larger than that of the undoped parent CQDs. Those fine changes can be correlated with the copper impurities, which induce optically active states and additional electron−nuclear spin interactions. Natural-abundance copper contains 69% ^{63}Cu and 31% ^{65}Cu, both having an $I = 3/2$ nuclear spin. This will be corroborated by the spin Hamiltonian simulations.

To further explore the dependence of the luminescence on the spin properties of the carriers, we monitored the dependence of the ODMR signals on the MW audio-modulation frequency. Such dependence is a Fourier transform of a time-resolved ODMR measurement, therefore revealing information about the spin-relaxation time. The relation depends on the spin's interaction with its immediate surroundings (e.g., free or trapped, spin−orbit coupling, or electron−nuclear coupling). Figure 3a,b portray representative CW-ODMR spectra of CdSe/CdS and Cu@CdSe/CdS CQDs, respectively, recorded under variable audio-modulation frequencies. The CW-ODMR resonances were fitted by two Gaussian functions, and their integrated areas were plotted (symbols) versus the MW audio-modulation frequency, as shown in Figure 3c,d for the undoped and doped-CQDs, respectively. The evolutions of the spectra in Figure 3a,b, as well as the curves in Figure 3c,d exhibit common trends. The absolute IP intensity of the narrow and broad components increases from the lowest frequency up to an optimal point. Then, the trend is reversed. The optimal point occurs when the MW period (on−off) is commensurate with the spin-flip relaxation cycle. Below that point, the MW periods contain dead times, and above that point, a spin recovery is truncated. The OP curves also reach an optimal point, which is proportional to $1/T_1$. The dashed curves in Figure 3c,d are associated with kinetic simulations of spin dynamics under magnetic resonance conditions. From this kinetic model, the radiative and spin relaxation times can be extracted (see the theoretical section below). A comparison between the variables from CdSe/CdS and Cu-doped CdSe/CdS CQDs (Table 2) exposes compatible T_1 values for the narrow bands (the electron); however, there are apparent dissimilarities in the variables for the broad band (the hole). This further supports the involvement of the Cu site in the trapping of the hole carrier in Cu-doped CdSe/CdS CQDs.

CW-ODMR Spectra of $CuInS_2$ and $CuInS_2$/(CdS, ZnS) CQDs. Figure 4 depicts the ODMR spectra of ensembles of $CuInS_2$/ZnS (top), $CuInS_2$/CdS (middle), and $CuInS_2$ (bottom) CQDs. These spectra were recorded at 2.5 K while the differential intensity of the corresponding PL bands was monitored (see Figure 1) with Voigt alignment and an MW audio frequency of 880 Hz. In all samples, the IP ODMR curve comprises a broad and negative resonance centered at 0.4 T and another low-field resonance at ~0.2 T with the opposite sign. Comparing the set of spectra in Figure 4 uncovers a considerable similarity in their patterns, indicating that the carriers responsible for these magnetic resonance processes are insensitive to surface or interface defects and potential carrier delocalization across the core/shell interface. Thus, the resonance features in Figure 4 can be associated with the intrinsic properties of the $CuInS_2$ cores. The OP ODMR spectra of these copper-based CQDs are composed of the same components but have reduced intensity. The negative signal in the ODMR spectra of these copper-based CQDs indicates a situation in which $\tau_R \geq T_1$, suggesting localization of at least

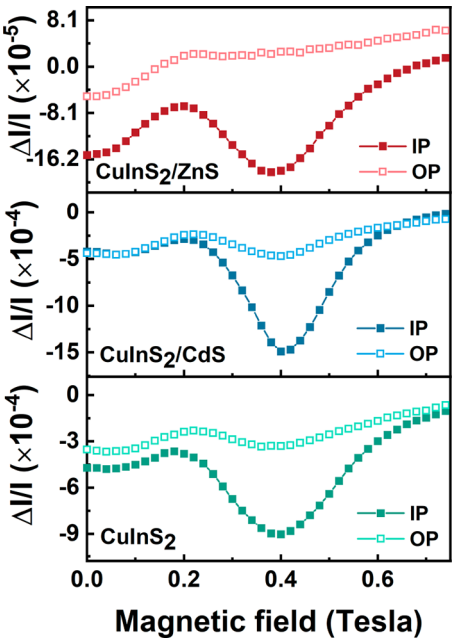

Figure 4. CW-ODMR spectra of $CuInS_2$/ZnS (top), $CuInS_2$/CdS (middle), and $CuInS_2$ (bottom) CQDs with a modulation frequency of 880 Hz. The measurements were acquired at 2.5 K under 405 nm laser excitation.

one carrier. Note that the resonances observed in Figure 4 sit on top of a nonresonant background, which may originate either from a parasitic electric field within the cavity or from a spin−orbit resonance.[56−58] A representative fit of this nonresonant background and an ODMR spectrum with a baseline correction is shown in Figure S3 in the Supporting Information. Notably, the low-field resonance (0.2 T) appears precisely at half the magnetic field of the higher field resonance (0.4 T), suggesting recombination from a triplet manifold, which will be further validated in the following discussion.

Representative CW-ODMR spectra of $CuInS_2$ and $CuInS_2$/CdS CQDs recorded in the Faraday configuration with circularly polarized detection are shown in Figure S4 in the Supporting Information and exhibit trends similar to those observed in the Voigt alignment, suggesting that the latter is comprised of the circularly polarized components. Therefore, the remaining discussions solely refer to the Voigt measurements.

Further investigation of the copper-based materials will be mainly on $CuInS_2$ because all of the ODMR signals of the copper-based samples show the same pattern. To further explore the dependence of the luminescence on paramagnetic centers with unpaired spins, we monitored the dependence of the ODMR signals on the MW audio-modulation frequency. Figure 5a depicts a representative set of CW-ODMR spectra of $CuInS_2$ CQDs monitored in the Voigt configuration, including IP and OP measurements with different MW audio frequencies. As the modulation frequency increases, the resonances at both 0.2 and 0.4 T increase, further supporting the involvement of a triplet state. Figure 5b plots the resonances' integrated intensities versus the audio-modulation frequency when the IP and OP responses are monitored at 0.2 and 0.4 T. It is seen from Figure 5b that the singular points (minima in the IP trend and maxima in the OP trend) are only slightly shifted in their frequencies when they are measured at 0.2 or 0.4 T. The copper-based core/shell CQD samples show

https://doi.org/10.1021/acsnano.2c05130
ACS Nano 2022, 16, 12866−12877

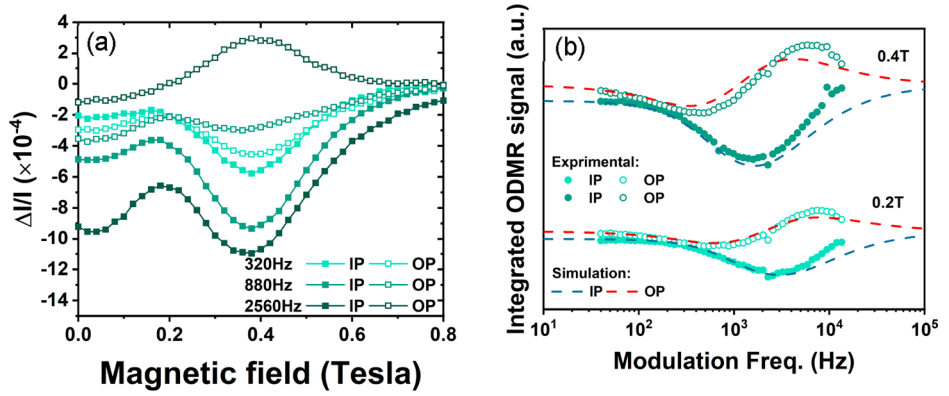

Figure 5. (a) Representative CW-ODMR spectra acquired at 2.5 K under 405 nm laser excitation at different modulation frequencies for $CuInS_2$ CQDs. (b) Integrated ODMR signal (IP and OP) versus the modulation frequency (log scale) for $CuInS_2$ CQDs at 0.4 (dark green) and 0.2 (light green) T. The red and blue dashed lines are fitted simulations to the IP and OP, respectively, according to the kinetic model shown in eq 2. The fit parameters are summarized in Table 2 and Table S1.

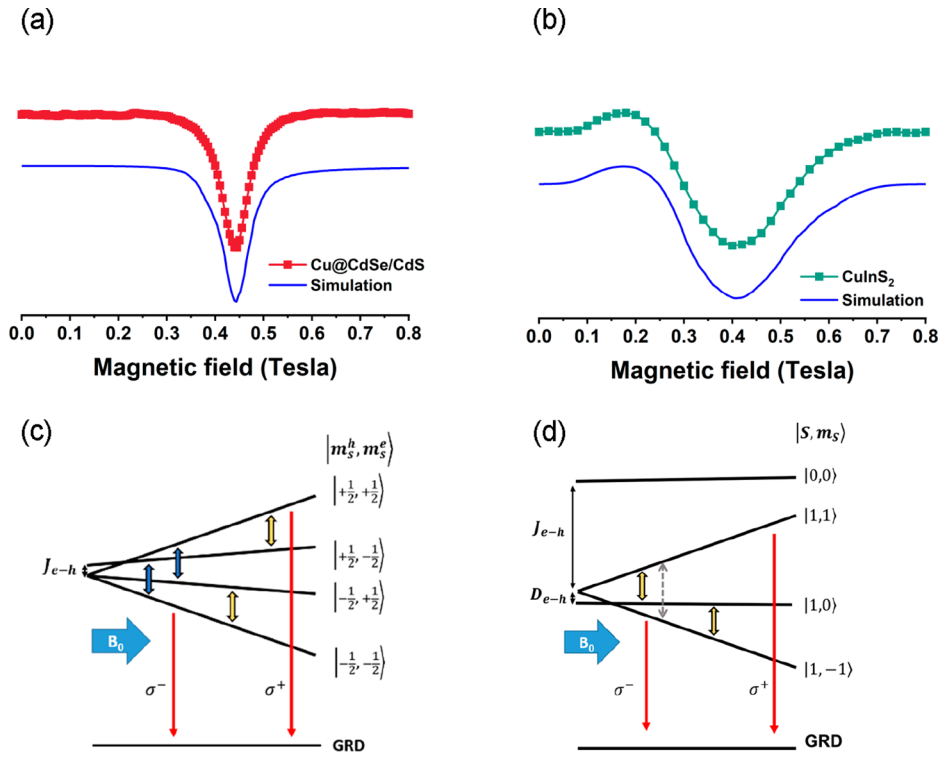

Figure 6. CW-ODMR spectra and fitted simulations (blue) of (a) Cu@CdSe/CdS and (b) $CuInS_2$ CQDs. The simulations were calculated using the spin Hamiltonian in eq 1, and the fit parameters are presented in Table 1. (c, d) Spin diagram models, according to the fitted simulations, demonstrating the magneto-optical transitions of Cu@CdSe/CdS and $CuInS_2$ CQDs, respectively. The red arrows represent the emission from the emitting levels to the ground state, the bold blue and yellow arrows represent the magnetic resonance transitions through microwave irradiation for the hole and electrons, respectively, and the gray dashed arrow in (d) represents the forbidden transition $\Delta m_S = \pm 2$.

the same behavior with the modulation frequency (see Figure S5 for further discussion). The trends in Figure 5b were simulated using kinetic equations, including the generation of carriers, radiative recombination, spin-relaxation, and inter-system crossing (see the model below).

The association of these ODMR signals with the emission processes was verified by recording the spectral dependence (SD) ODMR spectrum for $CuInS_2$ CQDs, involving a scan of a PL spectrum under the influence of a magnetic resonance condition. A representative SD-ODMR curve for the $CuInS_2$ CQDs recorded at 0.4 T is compared to the PL spectrum in Figure S6. The SD-ODMR and PL curves overlap on the low-energy side, suggesting some complexity in the PL band itself. Previous work[59,60] has shown a time-dependent red shift of the $CuInS_2$ CQD PL over the first ~100 ns that may relate to this observation. In any case, the ODMR signals reported here primarily represent the redder spectral region of the CW PL spectrum.

The following discussion deals with interpreting the ODMR observations on the basis of a spin Hamiltonian and a kinetic model. Figure 6a,b compares the experimental ODMR spectra of copper-doped and copper-based CQDs. This comparison

https://doi.org/10.1021/acsnano.2c05130
ACS Nano 2022, 16, 12866−12877

Table 1. Best-Fit Parameters for Simulating the ODMR Spectra on the Basis of the Spin Hamiltonian Model of Eq 1

	CdSe/CdS	Cu@CdSe/CdS	$CuInS_2$
S_e	1/2	1/2	1/2
$S_{h(t)}$	1/2	1/2	1/2
g_e	$g_{xx} = g_{yy} = g_{zz} = 1.72$	$g_{xx} = g_{yy} = 1.73$, $g_{zz} = 1.74$	$g_{xx} = g_{yy} = 1.81$, $g_{zz} = 1.96$
$g_{h(t)}$	$g_{xx} = g_{yy} = 1.83$, $g_{zz} = 2.3$	$g_{xx} = g_{yy} = 1.76$, $g_{zz} = 1.91$	
J_{e-h} (μeV)	0.1	0.1	1 meV
D (μeV)			19
$A_{h\text{-}Cu}$ (μeV)		2.4	
$A_{e\text{-}Cu}$ (μeV)		0.6	
$A_{e,h-In}$ (μeV)			3.8

Table 2. Kinetic Model (Eq 2) Variables Derived from Simulations of ODMR Modulation Frequency Dependence

	CdSe/CdS		Cu@CdSe/CdS		$CuInS_2$	
	broad (h)	narrow (e^-)	broad (h)	narrow (e^-)	peak 0.2 T	peak 0.4 T
r_s (s^{-1})	8×10^4	5×10^3	2×10^4	3×10^3	1.3×10^4	8×10^3
r_t (s^{-1})	1×10^3	9×10^2	1×10^2	1×10^1	1×10^2	1×10^2
T_1 (s)	6.1×10^{-5}	6.6×10^{-4}	1.1×10^{-4}	8.2×10^{-4}	1.3×10^{-4}	2.3×10^{-4}

highlights the differences in their resonance positions and subcomponents. To complete the analysis of the different recombination mechanisms, the following sections thoroughly discuss spin-manifold models, which can explain the diversity of the experimental results. The ODMR spectrum of the Cu-doped II–VI CQDs reflects the flip of individual spins; thus indicating a conduction-band electron (or shallow donor state) with spin $S_e = 1/2$, a trapped hole with spin $S_h = 1/2$, and a relatively weak electron–hole exchange interaction, as described by the spin diagram in Figure 6c. The red arrows in Figure 6c indicate the radiative recombination processes, while the magnetic resonance transitions of the hole and electron are presented by bold blue and yellow arrows, respectively. The ODMR spectrum of the I–III–VI_2 CQDs shows correlated resonances, indicating relatively strong electron–hole exchange coupling ($J_{e\text{-}h}$) that generates singlet ($S = 0$, $m_S = 0$) and triplet ($S = 1$, $m_S = \pm 1, 0$) states. The data further indicate a small axial zero-field splitting (D) of the triplet manifold into its $m_S = 0$ and $m_S = \pm 1$ components. The yellow arrows in Figure 6d indicate the allowed magnetic resonance transitions ($\Delta m_S = \pm 1$), and the dashed gray arrow refers to the formally forbidden half-field transition ($\Delta m_S = 2$).

In the generic diagrams shown in Figure 6c,d, recombination from the bright ± 1 states effectively depletes their population instantly when $\tau_R < T_1$, while magnetic resonance transitions recover their population: viz., leading to a net increase in the luminescence intensity ($\Delta I/I > 0$). However, when $\tau_R \geq T_1$, the Boltzmann distribution creates a situation in which a population difference between the bright and dark states is reversed, for which a magnetic resonance can decrease the population of an emitting state ($\Delta I/I < 0$), generating a negative ODMR signal. In the present study, the IP ODMR spectra were dominated by negative signals, hence reflecting recombination processes in which at least one carrier is trapped at a localized site and dictates a long radiative lifetime. The experimental data were simulated using spin Hamiltonian calculations based on the generic diagrams discussed above. The best-fit curves obtained from these simulations are shown by the blue lines in Figure 6a,b. The temporal responses measured in the frequency domain (Figures 3 and 5) were replicated by the kinetic model discussed below.

The observed ODMR spectra shown in Figure 6a,b were simulated via the use of the following spin Hamiltonian:

$$H_s = \mu_B \vec{S}_{e(t)} \bar{\bar{g}}_{e(t)} \vec{B}_0 + \mu_B \vec{S}_{h(t)} \bar{\bar{g}}_{h(t)} \vec{B}_0 + J_{e\text{-}h} \vec{S}_{e(t)} \vec{S}_{h(t)} + \bar{\bar{D}}_{e\text{-}h} \vec{S}_{e(t)} \vec{S}_{h(t)} + A \vec{S}_{e(t),h(t)} \vec{I}_j \quad (1)$$

The first two terms in eq 1 correspond to the Zeeman interactions of a free or trapped electron ($S_{e(t)}$, t = trap) and hole ($S_{h(t)}$). The $g_{e(t),h(t)}$ factors are proportional constants, correlating spin quantum numbers, $S_{e(t),h(t)}$, with their magnetic moments. It is important to note that $g_{e(t),h(t)}$ values differ from the Landé g factor, which is associated with the total angular momentum (spin–orbit). The latter tolerates either a positive or negative sign. Although a valence-band hole in II–VI compounds demands the consideration of a Landé g factor, the analysis below proposes the involvement of trapped holes; hence, the discussion refers to their pure spin variables.

The third term in eq 1 describes the electron–hole ($J_{e\text{-}h}$) spin exchange coupling, while the fourth term describes the zero-field splitting (D). The last term describes the hyperfine interaction (A) between photogenerated carrier spins and nuclear spins (I_j) in close proximity. The simulated spectra are displayed in Figures 6a,b, and the spin-Hamiltonian parameters used to generate these spectra are summarized in Table 1.

In addition, the ODMR patterns' dependence on the MW audio frequency in Figures 3 and 5 were simulated using a kinetic model, given by the equations[52]

$$\frac{dn_s}{dt} = G_s - C_s n_s + k_{MW}(n_t - n_s) - k_{ISC}(n_s - F n_s) + k_{ISC}(n_t - (1 - F) n_t)$$

$$\frac{dn_t}{dt} = G_t - C_t n_t + k_{MW}(n_s - n_t) - k_{ISC}(n_t - (1 - F) n_t) + k_{ISC}(n_s - F n_s)$$

$$F = (1 + e^{\Delta E/kT})^{-1}; \; C_{s,t} = r_{s,t} + d_{s,t}; \; I \propto r_s n_s + r_t n_t \quad (2)$$

where n_t and n_s are the populations of triplet ($S = 1$, $m_S = \pm 1$, 0) and singlet ($S = 0$) spin sublevels, respectively, G_t and G_s are the generation rates, d_t and d_s are the dissociation rate constants, r_t and r_s are the recombination rate constants, k_{MW}

https://doi.org/10.1021/acsnano.2c05130
ACS Nano 2022, 16, 12866–12877

represents the rate constant of the magnetic resonance transitions, k_{ISC} is the intersystem-crossing rate constant (spin mixing term), F is a Fermi−Dirac thermal distribution function, and ΔE refers to a resonance transition energy. Implementing the expressions in eq 2 for simulation of the ODMR resonance intensities versus modulation frequency trends leads to the complete set of parameters given in Table S1. The most significant parameters are summarized in Table 2. The spin relaxation time, T_1, was extracted from the extrema of the integrated OP signal. As explained above, at this point the MW modulation frequency is proportional to $1/T_1$. The best-fit trends using eq 2 are plotted as dashed lines in Figures 3 and 5.

The simulations of the CW- and the temporal-ODMR observations exposed a few interesting features. In II−VI CQDs, the g factors of the electrons in undoped and doped CdSe/CdS are quite close to each other (the spin Hamiltonian simulations for the undoped CdSe/CdS CQDs are given in Figure S7a in the Supporting Information). The g_e value of ∼1.7 found here is compatible with that of an electron in the conduction band of CdSe/CdS CQDs with a quasi-type-II band alignment and delocalization of the electron across the CdSe/CdS interface.[53,61] g_h, on the other hand, varies significantly from the undoped to the doped CdSe/CdS CQD samples, suggesting the introduction of Cu^{2+} into the recombination process. In contrast to the Landé g_h factor in CdSe, where the hole has a negative value caused by the spin−orbit interaction,[62] g_h values for doped and undoped CdSe/CdS CQDs, derived from the analysis of the ODMR observations, have a positive value close to the value of a free carrier (∼2.0). Such a value implies an s or d character of the ground state with a weak spin−orbit interaction. A previous ODMR study of undoped CdSe/CdS CQDs[53] uncovered hole trapping at twin boundary or edge dislocations along the CdSe/CdS interface (e.g., V_{Cd} acceptors). The present Cu@CdSe/CdS CQDs were prepared by partial cation exchange starting from preformed CdSe/CdS CQDs, and it is envisioned that the copper impurities can fill such vacancies at the CdSe/CdS interface. Furthermore, the resonance width of Cu@CdSe/CdS CQDs required using a hyperfine interaction emanating from the I = 3/2 copper nucleus, predominantly around the hole carrier, implying its proximity to a copper ion. The hyperfine constant (2.4 μeV) is on the same order of magnitude as the hyperfine splitting for Cu^{2+} (S = 1/2, I = 3/2) in the ground state.[63] Hence, the results indicate that the deep emission in these Cu@CdSe/CdS CQDs is associated with recombination of a conduction-band electron with a copper-localized hole associated with paramagnetic Cu^{2+} ($3d^9$, S = 1/2) positioned at a cation site (Cu_{Cd}). As discussed above, the two components in the ODMR spectra (narrow and broad) vary differently with the modulation frequency; therefore, they carry individual spins compatible with the diagram in Figure 6c, representing the weak electron−hole exchange regime. Moreover, the kinetic simulations exposed different spin-relaxation times, T_1, for the electron and hole (Table 2) and a pronounced change of the hole relaxation time upon doping with copper ions. Those temporal effects further support individual spin-flip processes in the undoped and doped CQDs: viz., a singlet nature of the recombination emission. We note that the estimated electron−hole exchange constant ($J_{e\text{-}h}$ ≈ 0.1 μeV) deduced from these data is substantially smaller than that found previously in core-only Cu-doped CdSe CQDs ($J_{e\text{-}h}$ = 0.85 meV, d = 3.2 nm).[28] This inconsistency likely originates from the fact that the current core/shell CQDs differ from those core-only CQDs in multiple critical ways that all reduce $J_{e\text{-}h}$. First, electron delocalization across the CdSe/CdS heterointerface increases the carrier's volume in core/shell CQDs relative to core-only CQDs, leading to a weaker pairwise electron−hole spin-exchange than would be found in core-only CQDs of the same diameter.[64] The overall diameter of the Cu@CdSe/CdS CQDs studied here is ∼5.2 nm (see the Supporting Information), in comparison to only 3.2 nm in ref 28. Second, the partial-cation-exchange synthesis method used here likely yields a nonstatistical dopant distribution that favors copper placement at the CdSe/CdS interface (filling V_{Cd} defects), or even preferentially within the CdS shell,[65] both of which would reduce $J_{e\text{-}h}$ substantially relative to isotropic doping of core-only CdSe CQDs.

With copper-based compounds, the g factors of $CuInS_2$ and $CuInS_2$/(CdS, ZnS) CQDs differ from those of Cu-doped II−VI materials, showing an average value of $g \approx 2.0$ for the 0.40 T resonance, with evidence of a slight axial distortion. Such a g value is consistent with localized carriers at a trigonally distorted Cu^{2+} site in the luminescent excited state of these $CuInS_2$ CQDs.[14,66,67] The resonance centered around 0.2 T occurs at a half-field value of that at 0.4 T, unambiguously supporting a triplet manifold scenario and the spin diagram displayed in Figure 6d. Hence, the low-field resonance corresponds to a formally forbidden transition by the spin selection rules (Δm_S = 2), which gains some limited intensity via the state crossing at low fields. This level crossing may be the source of this signal's sign inversion at higher fields. Notably, a similar anomalous behavior at low magnetic fields appeared previously in the magneto-PL (MCPL) of $CuInS_2$ CQDs,[28] in correspondence with state mixing as proposed here. A similar level crossing within an axially zero field split triplet spin manifold has also previously been deduced from ODMR measurements of Cu-doped GaP single crystals.[18] Triplet manifold formation is further supported by the large electron−hole exchange coupling ($J_{e\text{-}h}$ ≈ 1 meV) obtained from the simulation, with a surplus crystal field contribution (D ≈ 19.0 μeV). The latter emanates from a local distortion around a Cu^{2+} site generated after the capture of a photogenerated hole by Cu^+. A previous variable-temperature lifetime and MCPL study of similar $CuInS_2$ CQDs revealed a value close to the same electron−hole exchange coupling ($J_{e\text{-}h}$ = 1.1 meV) and also showed evidence of a small zero-field splitting within the triplet manifold, although the latter was not quantified.[28] Above all, the similar T_1 values found for the 0.4 and 0.2 T ODMR bands (with a slight deviation that can be correlated with the baseline correction) provide strong support for their assignment as transitions within the same triplet spin manifold.

Finally, Cu^{2+} and In^{3+} possess isotopes with nonzero nuclear spins of a high abundance, contributing to the substantial broadening of the ODMR signal of the $CuInS_2$ CQDs. Figure S7b in the Supporting Information displays a simulation performed without hyperfine coupling (with indium nuclei), highlighting the essential need to include it to achieve the observed line broadening. Notably, this effect is more pronounced in the ODMR of I−III−VI_2 CQDs with an occupation of 50% of the metal site with indium ions with 100% occurrence of nuclear spin I = 9/2 and a smaller contribution by the copper ions with spin I = 3/2. The simulations reflect an obvious need to include a superhyperfine

https://doi.org/10.1021/acsnano.2c05130
ACS Nano 2022, 16, 12866−12877

interaction between electrons and neighboring indium cations to best fit the resonance's width (see Table 1 and Figure S7b).

The $J_{e\text{-}h}$ value of $CuInS_2$ reflects the localization of both an electron and a hole in close proximity to enable their reasonably large spin-exchange interaction (~1 meV). The g values are compatible with hole localization at a Cu^{2+} site in the excited state,[67] but the electron position is less clear. One scenario enables the creation of a self-trapped exciton comprised of a conduction band electron that feels a localization potential induced by hole localization at a Cu site, both due to electrostatics and because of lattice strain following nuclear reorganization around the copper. In such a case, a conduction band electron in the proximity of a photogenerated Cu^{2+} ion may experience a superhyperfine coupling with a minimum of two surrounding In nuclei, with an overall contribution of ~3.8 μeV (i.e., each In nucleus contributes 1.9 μeV), suitable for a superhyperfine dipole−dipole coupling.[68−71] The simulations shown in Figure 6b and Figure S7b strongly support the model of a self-trapped exciton bound by the localization potential of the photogenerated Cu^{2+} center, with a weak influence of the surrounding indium atoms. Another scenario involves the trapping of a photogenerated electron in a shallow donor site related to In_{Cu}, In_i, or V_S defects in the case of In-rich samples.[72,73] However, this scenario can be ruled out, since Cu-rich and In-rich $CuInS_2$ CQD samples showed the same signal shape in ODMR (see Figure S8). Thus, a self-trapped exciton model coincides well with the ODMR observations discussed at length above. Such a model deviates significantly from that assigned to the copper-doped II−VI core/shell CQDs studied here and may emanate from fundamental differences in their electronic band structure and elemental compositions, as well as localization of Cu^+ dopants at interfaces in the core/shell CQDs.

CONCLUSIONS

In summary, the magneto-optical properties of Cu@CdSe/CdS, $CuInS_2$, and $CuInS_2$/(ZnS, CdS) CQDs have been studied using CW- and time-resolved ODMR spectroscopy. The ODMR spectra of Cu@CdSe/CdS CQDs showed two independent resonances with different spectroscopic appearances, g factors, and spin-relaxation times. Spin-Hamiltonian simulations revealed a weak electron−hole exchange interaction and selective hyperfine coupling of the hole to a Cu^{2+} nucleus. Thus, the results indicated a recombination process involving an electron delocalized across the core/shell interface with a hole localized at a Cu^{2+} center, resembling the ligand to metal charge transfer processes existing in molecules and in Cu@CdSe CQDs.[28] Interestingly, the ODMR of the $CuInS_2$ CQDs (with/without shells) substantially deviated from that of the Cu@CdSe/CdS CQDs, showing a dominant band at the midmagnetic field and an additional band at half the field of the first, with a mutual correlation between the two under temporal examination. These facts unambiguously verified the occurrence of a recombination emission from a triplet spin state. Spin-Hamiltonian simulations showed a strong electron−hole exchange interaction accompanied by a small axial zero-field splitting. Furthermore, the simulation reveals g factors close to that of a free carrier (~2.00), with a slight axial distortion, which is a conventional value for a trapped carrier. Such a value is typical for the Cu^{2+} center formed in such an excited state, with local distortion created by the trapping of a hole. Moreover, the simulation indicated a superhyperfine coupling of the electron with at least two indium nearest neighbors, suggesting localization of the electron close to the Cu^{2+} site. The resulting description of this luminescence thus involves recombination of a self-trapped exciton localized around the photogenerated Cu^{2+} center. Importantly, other possible carrier trapping sites are excluded for reasons justified in the main body of the manuscript. Overall, the study advanced the understanding of radiative recombination in copper-containing semiconductor CQDs, clarifying the oxidation states of the copper ions, and yielding a variety of previously unknown physical parameters with significant importance for future implementation of these materials in various optoelectronic and spin-related technologies.

METHODS

PL and ODMR Spectroscopy. ODMR measurements were carried out using a home-built ~10.8 GHz resonator with a window for laser irradiation placed in a Janis 12 CNDT liquid-helium cryostat with a superconducting coil for magnetic field sweep. The magnetic field was controlled by an Oxford IPS 120 power supply. The sample was excited by a continuous-wave (CW) laser diode with a wavelength of 405 nm. Microwave (MW) irradiation was generated by an HP 83620A source, triggered by a Stanford DG 535 pulse generator and amplified by a Narda West 60583 MW amplifier. After excitation and magnetic resonance occurrence, the ODMR signal was passed through a 450/532 nm long-pass filter, inserted into a monochromator (SpectraPro 300i spectrometer), and detected with a Si diode. The ODMR signal was recorded with an Ametek 7270 Lock-in amplifier referenced by on−off modulation of the MW (audio frequency of 0.02−20 kHz). ODMR experiments were performed in Voigt ($B_0 \perp$exc) and Faraday ($B_0 \parallel$exc) configurations, where a quarter waveplate and a linear polarizer were used to collect the right and left circularly polarized light in the latter. PL measurements were carried out in the same setup as for the ODMR, using a chopper wheel to modulate the laser before excitation. The samples were sealed in quartz capillaries using Parafilm under ambient conditions. All ODMR simulations were performed using MATLAB code following the spin Hamiltonian in eq 1, assuming the contribution of an ensemble of spins at 2.5 K under 10.8 GHz microwave irradiation.

ASSOCIATED CONTENT

Supporting Information

The Supporting Information is available free of charge at https://pubs.acs.org/doi/10.1021/acsnano.2c05130.

Room-temperature absorption and PL measurements, structural properties of CQDs, Gaussian fit of Cu-doped CdSe/CdS, nonresonant background, Faraday configuration measurements, modulation-dependent ODMR for $CuInS_2$/(CdS, ZnS) CQDs, spectral-dependence measurement for $CuInS_2$ CQDs, ODMR simulations for CdSe/CdS CQDs and $CuInS_2$ CQDs without hyperfine interaction, ODMR spectra of In- and Cu-rich $CuInS_2$ CQDs, kinetic model variables, and additional sample details (PDF)

AUTHOR INFORMATION

Corresponding Authors

Daniel R. Gamelin − *Department of Chemistry, University of Washington, Seattle, Washington 98195-1700, United States;* orcid.org/0000-0003-2888-9916; Email: gamelin@uw.edu

Celso de Mello Donegá − *Condensed Matter and Interfaces, Debye Institute for Nanomaterials Science, Utrecht University, 3584 CC Utrecht, The Netherlands;*

https://doi.org/10.1021/acsnano.2c05130
ACS Nano 2022, 16, 12866−12877

orcid.org/0000-0002-4403-3627; Email: c.demello-donega@uu.nl

Efrat Lifshitz − *Schulich Faculty of Chemistry, Solid State Institute, Russell Berrie Nanotechnology Institute, Technion−Israel Institute of Technology, Haifa 3200003, Israel;* orcid.org/0000-0001-7387-7821; Email: ssefrat@technion.ac.il

Authors

Adi Harchol − *Schulich Faculty of Chemistry, Solid State Institute, Russell Berrie Nanotechnology Institute, Technion−Israel Institute of Technology, Haifa 3200003, Israel;* orcid.org/0000-0001-8401-8838

Yahel Barak − *Schulich Faculty of Chemistry, Solid State Institute, Russell Berrie Nanotechnology Institute, Technion−Israel Institute of Technology, Haifa 3200003, Israel*

Kira E. Hughes − *Department of Chemistry, University of Washington, Seattle, Washington 98195-1700, United States;* orcid.org/0000-0001-6454-8700

Kimberly H. Hartstein − *Department of Chemistry, University of Washington, Seattle, Washington 98195-1700, United States*

Huygen j. Jöbsis − *Condensed Matter and Interfaces, Debye Institute for Nanomaterials Science, Utrecht University, 3584 CC Utrecht, The Netherlands;* orcid.org/0000-0002-7417-1246

P. Tim Prins − *Condensed Matter and Interfaces, Debye Institute for Nanomaterials Science, Utrecht University, 3584 CC Utrecht, The Netherlands;* orcid.org/0000-0002-8258-0074

Complete contact information is available at: https://pubs.acs.org/10.1021/acsnano.2c05130

Author Contributions

‖A. H. and Y.B. contributed equally.

Notes

The authors declare no competing financial interest.

ACKNOWLEDGMENTS

E.L. and D.R.G. acknowledge the USA/Israel Binational Science Foundation (No. 2016156 and No. 2020076). E.L. acknowledges partial support from the joint USA National Science Foundation− USA/Israel Binational Science Foundation (NSF-BSF, No. 2017637) and from the Israel Science Foundation (No. 2528/19 and No. 1045/17). D.R.G. acknowledges partial support of this research from the UW Molecular Engineering Materials Center (DMR-1719797), an NSF Materials Research Science and Engineering Center. Additional support from the NSF (DMR-1807394 to D.R.G.) is gratefully acknowledged. C.d.M.D. acknowledges support by The Netherlands Organization for Scientific Research (NWO; grant 14614 "Q-Lumicon"). The authors are grateful to Dr. Kusha Sharma and Dr. Faris Horani for their assistance in editing.

REFERENCES

(1) Beaulac, R.; Schneider, L.; Archer, P. I.; Bacher, G.; Gamelin, D. R. Light-Induced Spontaneous Magnetization in Doped Colloidal Quantum Dots. *Science (80-.)* **2009**, *325*, 973−976.

(2) Beaulac, R.; Ochsenbein, S. T.; Gamelin, D. R. Colloidal Transition-Metal-Doped Quantum Dots. In *Nanocrystal Quantum Dots*; Victor, I. K., Ed.; CRC Press: 2010; pp 397−453.

(3) Karan, N. S.; Sarma, D. D.; Kadam, R. M.; Pradhan, N. Doping Transition Metal (Mn or Cu) Ions in Semiconductor Nanocrystals. *J. Phys. Chem. Lett.* **2010**, *1*, 2863−2866.

(4) Knowles, K. E.; Hartstein, K. H.; Kilburn, T. B.; Marchioro, A.; Nelson, H. D.; Whitham, P. J.; Gamelin, D. R. Luminescent Colloidal Semiconductor Nanocrystals Containing Copper: Synthesis, Photophysics, and Applications. *Chem. Rev.* **2016**, *116*, 10820−10851.

(5) Viswanatha, R.; Brovelli, S.; Pandey, A.; Crooker, S. A.; Klimov, V. I. Copper-Doped Inverted Core/Shell Nanocrystals with "Permanent" Optically Active Holes. *Nano Lett.* **2011**, *11*, 4753−4758.

(6) Van Der Stam, W.; Berends, A. C.; De Mello Donega, C. Prospects of Colloidal Copper Chalcogenide Nanocrystals. *ChemPhysChem* **2016**, *17*, 559−581.

(7) Panthani, M. G.; Akhavan, V.; Goodfellow, B.; Schmidtke, J. P.; Dunn, L.; Dodabalapur, A.; Barbara, P. F.; Korgel, B. A. Synthesis of CuInS2, CuInSe2, and Cu(InxGa1-x)Se2 (CIGS) Nanocrystal "Inks" for Printable Photovoltaics. *J. Am. Chem. Soc.* **2008**, *130*, 16770−16777.

(8) Bradshaw, L. R.; Knowles, K. E.; McDowall, S.; Gamelin, D. R. Nanocrystals for Luminescent Solar Concentrators. *Nano Lett.* **2015**, *15*, 1315−1323.

(9) Meinardi, F.; McDaniel, H.; Carulli, F.; Colombo, A.; Velizhanin, K. A.; Makarov, N. S.; Simonutti, R.; Klimov, V. I.; Brovelli, S. Highly Efficient Large-Area Colourless Luminescent Solar Concentrators Using Heavy-Metal-Free Colloidal Quantum Dots. *Nat. Nanotechnol.* **2015**, *10*, 878−885.

(10) Knowles, K. E.; Kilburn, T. B.; Alzate, D. G.; McDowall, S.; Gamelin, D. R. Bright CuInS2/CdS Nanocrystal Phosphors for High-Gain Full-Spectrum Luminescent Solar Concentrators. *Chem. Commun.* **2015**, *51*, 9129−9132.

(11) Yu, J.; Sharma, M.; Li, M.; Delikanli, S.; Sharma, A.; Taimoor, M.; Altintas, Y.; McBride, J. R.; Kusserow, T.; Sum, T. C.; Demir, H. V.; Dang, C. Low-Threshold Lasing from Copper-Doped CdSe Colloidal Quantum Wells. *Laser Photonics Rev.* **2021**, *15*, 2100034.

(12) Liu, Z.; Lu, X.; Chen, D. Photoelectrochemical Water Splitting of CuInS2 Photocathode Collaborative Modified with Separated Catalysts Based on Efficient Photogenerated Electron-Hole Separation. *ACS Sustain. Chem. Eng.* **2018**, *6*, 10289−10294.

(13) Aldakov, D.; Lefrançois, A.; Reiss, P. Ternary and Quaternary Metal Chalcogenide Nanocrystals: Synthesis, Properties and Applications. *J. Mater. Chem. C* **2013**, *1*, 3756−3776.

(14) Corrado, C.; Jiang, Y.; Oba, F.; Kozina, M.; Bridges, F.; Zhang, J. Z. Synthesis, Structural, and Optical Properties of Stable ZnS:Cu,Cl Nanocrystals. *J. Phys. Chem. A* **2009**, *113*, 3830−3839.

(15) Suzuki, A.; Shionoya, S. Mechanism of the Green-Copper Luminescence in ZnS Crystals. I. Direct Evidence for the Pair Emission Mechanism. *J. Phys. Soc. Jpn.* **1971**, *31*, 1455−1461.

(16) Yen, W. M.; Shionoya, S.; Yamamoto, H. *Fundamentals of Phosphors*; CRC Press: 2007.

(17) Broser, I.; Hoffmann, A.; Heitz, R.; Thurian, P. Zeeman and Piezospectroscopy of the Cu2+-Center in CdS. *J. Lumin.* **1991**, *48−49*, 693−697.

(18) Depinna, S.; Cavenett, B. C.; Killoran, N.; Monemar, B. Optically-Detected-Magnetic-Resonance Investigation of Triplet-Exciton Recombination at 1.91 EV in GaP:Cu. *Phys. Rev. B* **1981**, *24*, 6740−6743.

(19) Godlewski, M.; Lamb, W. E.; Cavenett, B. C. ODMR Investigation of Recombination Processes In ZnSe:Cu. *Solid State Commun.* **1981**, *39*, 595−599.

(20) Du, J.; Du, Z.; Hu, J. S.; Pan, Z.; Shen, Q.; Sun, J.; Long, D.; Dong, H.; Sun, L.; Zhong, X.; Wan, L. J. Zn-Cu-In-Se Quantum Dot Solar Cells with a Certified Power Conversion Efficiency of 11.6%. *J. Am. Chem. Soc.* **2016**, *138*, 4201−4209.

(21) Pan, Z.; Shen, Q.; Zhang, H.; Li, Y.; Zhao, K.; Wang, J.; Zhong, X.; Bisquert, J. High-Efficiency "Green" Quantum Dot Solar Cells. *J. Am. Chem. Soc.* **2014**, *136*, 9203−9210.

(22) Jaffe, J. E.; Zunger, A. Electronic Structure of the Ternary Chalcopyrite Semiconductors CuAlS2, CuGaS2, CuInS2, CuAlSe2,

CuGaSe2, and CuInSe2. *Condens. Matter Mater. Phys.* **1983**, *28*, 5822−5847.
(23) Soni, A.; Gupta, V.; Arora, C. M.; Dashora, A.; Ahuja, B. L. Electronic Structure and Optical Properties of CuGaS2 and CuInS2 Solar Cell Materials. *Sol. Energy* **2010**, *84*, 1481−1489.
(24) Binsma, J. J. M.; Giling, L. J.; Bloem, J. Luminescence of CuInS2. The Broad Band Emission and Its Dependence on the Defect Chemistry. *J. Lumin.* **1982**, *27*, 35−53.
(25) Ueng, H. Y.; Hwang, H. L. The Defect Structure of CuInS2. Part I: Intrinsic Defects. *J. Phys. Chem. Solids* **1989**, *50*, 1297−1305.
(26) Berends, A. C.; Mangnus, M. J. J.; Xia, C.; Rabouw, F. T.; De Mello Donega, C. Optoelectronic Properties of Ternary I-III-VI 2 Semiconductor Nanocrystals: Bright Prospects with Elusive Origins. *J. Phys. Chem. Lett.* **2019**, *10*, 1600−1616.
(27) Yadav, A. N.; Singh, A. K.; Chauhan, D.; Solanki, P. R.; Kumar, P.; Singh, K. Evaluation of Dopant Energy and Stokes Shift in Cu-Doped CdS Quantum Dots: Via Spectro-Electrochemical Probing. *New J. Chem.* **2020**, *44*, 13529−13533.
(28) Knowles, K. E.; Nelson, H. D.; Kilburn, T. B.; Gamelin, D. R. Singlet-Triplet Splittings in the Luminescent Excited States of Colloidal Cu+:CdSe, Cu+:InP, and CuInS2 Nanocrystals: Charge-Transfer Configurations and Self-Trapped Excitons. *J. Am. Chem. Soc.* **2015**, *137*, 13138−13147.
(29) Srivastava, B. B.; Jana, S.; Pradhan, N. Doping Cu in Semiconductor Nanocrystals: Some Old and Some New Physical Insights. *J. Am. Chem. Soc.* **2011**, *133*, 1007−1015.
(30) Grandhi, G. K.; Tomar, R.; Viswanatha, R. Study of Surface and Bulk Electronic Structure of II−VI Semiconductor Nanocrystals Using Cu as a Nanosensor. *ACS Nano* **2012**, *6*, 9751−9763.
(31) Zang, H.; Li, H.; Makarov, N. S.; Velizhanin, K. A.; Wu, K.; Park, Y. S.; Klimov, V. I. Thick-Shell CuInS2/ZnS Quantum Dots with Suppressed "Blinking" and Narrow Single-Particle Emission Line Widths. *Nano Lett.* **2017**, *17*, 1787−1795.
(32) Nelson, H. D.; Li, X.; Gamelin, D. R. Computational Studies of the Electronic Structures of Copper-Doped CdSe Nanocrystals: Oxidation States, Jahn−Teller Distortions, Vibronic Bandshapes, and Singlet−Triplet Splittings. *J. Phys. Chem. C* **2016**, *120*, 5714−5723.
(33) Mocatta, D.; Cohen, G.; Schattner, J.; Millo, O.; Rabani, E.; Banin, U. Heavily Doped Semiconductor Nanocrystal Quantum Dots. *Science (80-.)* **2011**, *332*, 77−81.
(34) Leach, A. D. P.; Shen, X.; Faust, A.; Cleveland, M. C.; La Croix, A. D.; Banin, U.; Pantelides, S. T.; Macdonald, J. E. Defect Luminescence from Wurtzite CuInS2 Nanocrystals: Combined Experimental and Theoretical Analysis. *J. Phys. Chem. C* **2016**, *120*, 5207−5212.
(35) Leach, A. D. P.; Macdonald, J. E. Optoelectronic Properties of CuInS2 Nanocrystals and Their Origin. *J. Phys. Chem. Lett.* **2016**, *7*, 572−583.
(36) Batabyal, S. K.; Tian, L.; Venkatram, N.; Ji, W.; Vittal, J. J. Phase-Selective Synthesis of CuInS2 Nanocrystals. *J. Phys. Chem. C* **2009**, *113*, 15037−15042.
(37) Rice, W. D.; Mcdaniel, H.; Klimov, V. I.; Crooker, S. A. Magneto-Optical Properties of CuInS2 Nanocrystals. *J. Phys. Chem. Lett.* **2014**, *5*, 4105−4109.
(38) Fuhr, A. S.; Yun, H. J.; Makarov, N. S.; Li, H.; McDaniel, H.; Klimov, V. I. Light Emission Mechanisms in CuInS2 Quantum Dots Evaluated by Spectral Electrochemistry. *ACS Photonics* **2017**, *4*, 2425−2435.
(39) Pinchetti, V.; Lorenzon, M.; McDaniel, H.; Lorenzi, R.; Meinardi, F.; Klimov, V. I.; Brovelli, S. Spectro-Electrochemical Probing of Intrinsic and Extrinsic Processes in Exciton Recombination in I-III-VI2 Nanocrystals. *Nano Lett.* **2017**, *17*, 4508−4517.
(40) Berends, A. C.; Rabouw, F. T.; Spoor, F. C. M.; Bladt, E.; Grozema, F. C.; Houtepen, A. J.; Siebbeles, L. D. A.; De Mello Donegá, C. Radiative and Nonradiative Recombination in CuInS2 Nanocrystals and CuInS2-Based Core/Shell Nanocrystals. *J. Phys. Chem. Lett.* **2016**, *7*, 3503−3509.
(41) Shabaev, A.; Mehl, M. J.; Efros, A. L. Energy Band Structure of CuInS2 and Optical Spectra of CuInS2 Nanocrystals. *Phys. Rev. B - Condens. Matter Mater. Phys.* **2015**, *92*, 1−9.
(42) Anand, A.; Zaffalon, M. L.; Gariano, G.; Camellini, A.; Gandini, M.; Brescia, R.; Capitani, C.; Bruni, F.; Pinchetti, V.; Zavelani-Rossi, M.; Meinardi, F.; Crooker, S. A.; Brovelli, S. Evidence for the Band-Edge Exciton of CuInS2 Nanocrystals Enables Record Efficient Large-Area Luminescent Solar Concentrators. *Adv. Funct. Mater.* **2020**, *30*, 1906629.
(43) Jara, D. H.; Stamplecoskie, K. G.; Kamat, P. V. Two Distinct Transitions in CuxInS2 Quantum Dots. Bandgap versus Sub-Bandgap Excitations in Copper-Deficient Structures. *J. Phys. Chem. Lett.* **2016**, *7*, 1452−1459.
(44) Fuhr, A.; Yun, H. J.; Crooker, S. A.; Klimov, V. I. Spectroscopic and Magneto-Optical Signatures of Cu1+ and Cu2+ Defects in Copper Indium Sulfide Quantum Dots. *ACS Nano* **2020**, *14*, 2212−2223.
(45) Xia, C.; Tamarat, P.; Hou, L.; Busatto, S.; Meeldijk, J. D.; De Mello Donega, C.; Lounis, B. Unraveling the Emission Pathways in Copper Indium Sulfide Quantum Dots. *ACS Nano* **2021**, *15*, 17573−17581.
(46) Hinterding, S. O. M.; Mangnus, M. J. J.; Prins, P. T.; Jöbsis, H. J.; Busatto, S.; Vanmaekelbergh, D.; De Mello Donega, C.; Rabouw, F. T. Unusual Spectral Diffusion of Single CuInS2 Quantum Dots Sheds Light on the Mechanism of Radiative Decay. *Nano Lett.* **2021**, *21*, 658−665.
(47) Nelson, H. D.; Gamelin, D. R. Valence-Band Electronic Structures of Cu+-Doped ZnS, Alloyed Cu-In-Zn-S, and Ternary CuInS2 Nanocrystals: A Unified Description of Photoluminescence across Compositions. *J. Phys. Chem. C* **2018**, *122*, 18124−18133.
(48) Hughes, K. E.; Ostheller, S. R.; Nelson, H. D.; Gamelin, D. R. Copper's Role in the Photoluminescence of Ag1-XCuxInS2 nanocrystals, from Copper-Doped AgInS2(x ∼ 0) to CuInS2(x = 1). *Nano Lett.* **2019**, *19*, 1318−1325.
(49) Dehnel, J.; Barak, Y.; Meir, I.; Budniak, A. K.; Nagvenkar, A. P.; Gamelin, D. R.; Lifshitz, E. Insight into the Spin Properties in Undoped and Mn-Doped CdSe/CdS-Seeded Nanorods by Optically Detected Magnetic Resonance. *ACS Nano* **2020**, *14*, 13478−13490.
(50) Lifshitz, E.; Fradkin, L.; Glozman, A.; Langof, L. Optically Detected Magnetic Resonance Studies of Colloidal Semiconductor Nanocrystals. *Annu. Rev. Phys. Chem.* **2004**, *55*, 509−557.
(51) Hughes, K. E.; Hartstein, K. H.; Gamelin, D. R. Photodoping and Transient Spectroscopies of Copper-Doped CdSe/CdS Nanocrystals. *ACS Nano* **2018**, *12*, 718−728.
(52) Lee, S. Y.; Paik, S.; McCamey, D. R.; Boehme, C. Modulation Frequency Dependence of Continuous-Wave Optically/Electrically Detected Magnetic Resonance. *Phys. Rev. B - Condens. Matter Mater. Phys.* **2012**, *86*, 1−17.
(53) Lifshitz, E.; Glozman, A.; Litvin, I. D.; Porteanu, H. Optically Detected Magnetic Resonance Studies of the Surface/Interface Properties of II - VI. *J. Phys. Chem. B* **2000**, *104*, 10449−10461.
(54) Barak, Y.; Meir, I.; Shapiro, A.; Jang, Y.; Lifshitz, E. Fundamental Properties in Colloidal Quantum Dots. *Adv. Mater.* **2018**, *30*, 1801442.
(55) Lifshitz, E.; Brumer, M.; Kigel, A.; Sashchiuk, A.; Bashouti, M.; Sirota, M.; Galun, E.; Burshtein, Z.; Le Quang, A. Q.; Ledoux-Rak, I.; Zyss, J. Air-Stable PbSe/PbS and PbSe/PbSexS1-x Core/Shell Nanocrystal Quantum Dots and Their Applications. *J. Phys. Chem. B* **2006**, *110*, 25356−25365.
(56) Glozman, A.; Lifshitz, E. Optically Detected Spin and Spin-Orbital Resonance Studies of CdSe/CdS Core-Shell Nanocrystals. *Mater. Sci. Eng., C* **2001**, *15*, 17−19.
(57) Fradkin, L.; Langof, L.; Lifshitz, E.; Rogach, A.; Gaponik, N.; Weller, H.; Eychmüller, A. Magneto-Optical Studies of HgTe/HgxCd1-XTe(S) Core-Shell Nanocrystals. *ChemPhysChem* **2003**, *4*, 1203−1210.
(58) Gokhberg, K.; Glozman, A.; Lifshitz, E.; Maniv, T.; Schlamp, M. C.; Alivisatos, P. Electron (Hole) Paramagnetic Resonance of Spherical CdSe Nanocrystals. *J. Chem. Phys.* **2002**, *117*, 2909.

https://doi.org/10.1021/acsnano.2c05130
ACS Nano 2022, 16, 12866−12877

(59) Tran, T. K. C.; Le, Q. P.; Nguyen, Q. L.; Li, L.; Reiss, P. Time-Resolved Photoluminescence Study of CuInS2/ZnS Nanocrystals. *Adv. Nat. Sci. Nanosci. Nanotechnol.* **2010**, *1*, 025007.
(60) Sun, J.; Ikezawa, M.; Wang, X.; Jing, P.; Li, H.; Zhao, J.; Masumoto, Y. Photocarrier Recombination Dynamics in Ternary Chalcogenide CuInS2 Quantum Dots. *Phys. Chem. Chem. Phys.* **2015**, *17*, 11981−11989.
(61) Gupta, J. A.; Awschalom, D. D.; Efros, A. L.; Rodina, A. V. Spin Dynamics in Semiconductor Nanocrystals. *Phys. Rev. B* **2002**, *66*, 125307.
(62) Liu, F.; Biadala, L.; Rodina, A. V.; Yakovlev, D. R.; Dunker, D.; Javaux, C.; Hermier, J.-P.; Efros, A. L.; Dubertret, B.; Bayer, M. Spin Dynamics of Negatively Charged Excitons in CdSe/CdS Colloidal Nanocrystals. *Phys. Rev. B* **2013**, *88*, 35302.
(63) Thirumala Rao, G.; Babu, B.; Joyce Stella, R.; Pushpa Manjari, V.; Ravikumar, R. V. S. S. N. Spectral Investigations on Undoped and Cu2+ Doped ZnO-CdS Composite Nanopowders. *Spectrochim. Acta - Part A Mol. Biomol. Spectrosc.* **2015**, *139*, 86−93.
(64) Brovelli, S.; Schaller, R. D.; Crooker, S. A.; García-Santamaría, F.; Chen, Y.; Viswanatha, R.; Hollingsworth, J. A.; Htoon, H.; Klimov, V. I. Nano-Engineered Electron−Hole Exchange Interaction Controls Exciton Dynamics in Core−Shell Semiconductor Nanocrystals. *Nat. Commun.* **2011**, *2*, 280.
(65) Archer, P. I.; Santangelo, S. A.; Gamelin, D. R. Inorganic Cluster Syntheses of TM2+-Doped Quantum Dots (CdSe, CdS, CdSe/CdS): Physical Property Dependence on Dopant Locale. *J. Am. Chem. Soc.* **2007**, *129*, 9808−9818.
(66) Godlewski, M.; Lamb, W. E.; Cavenett, B. C. ODMR Investigations of IR Photoluminescence in ZnS:Cu. *J. Phys. C Solid State Phys.* **1982**, *15*, 3925−3942.
(67) Poolton, N. R. J.; Smith, G. M.; Riedi, P. C.; Allen, J. W.; Firth, A. V.; Cole-Hamilton, D. J.; McInnes, E. J. L. Appearance of Copper D9 Defect Centres in Wide-Gap CdSe Nanoparticles: A High-Frequency EPR Study. *Phys. Status Solidi Basic Res.* **2005**, *242*, 829−835.
(68) Schlegel, C.; Van Slageren, J.; Timco, G.; Winpenny, R. E. P.; Dressel, M. Origin of Superhyperfine Interactions in the Anti-ferromagnetic Ring Cr 7Ni. *Phys. Rev. B - Condens. Matter Mater. Phys.* **2011**, *83*, 5−7.
(69) von Bardeleben, H.J. Identification of the Phosphor Vacancy in Electron Irradiated P-Type InP. *Solid State Commun.* **1986**, *57*, 137−139.
(70) Peeks, M. D.; Tait, C. E.; Neuhaus, P.; Fischer, G. M.; Hoffmann, M.; Haver, R.; Cnossen, A.; Harmer, J. R.; Timmel, C. R.; Anderson, H. L. Electronic Delocalization in the Radical Cations of Porphyrin Oligomer Molecular Wires. *J. Am. Chem. Soc.* **2017**, *139*, 10461−10471.
(71) Augustyniak-JabŁokow, M. A.; Jacyna-Onyszkiewicz, I.; Ivanova, T. A.; Polovniak, V. K.; Shustov, V. A.; Yablokov, Y. V. Derealization of the Cu2+ Unpaired Electron on the next Nearest Ligands in Sr2Pd0.99Cu0.01O3 Ceramics. *Acta Phys. Polym., A* **2008**, *114*, 197−201.
(72) Liu, W.; Zhang, Y.; Zhao, J.; Feng, Y.; Wang, D.; Zhang, T.; Gao, W.; Chu, H.; Yin, J.; Wang, Y.; Zhao, J.; Yu, W. W. Photoluminescence of Indium-Rich Copper Indium Sulfide Quantum Dots. *J. Lumin.* **2015**, *162*, 191−196.
(73) Omata, T.; Nose, K.; Kurimoto, K.; Kita, M. Electronic Transition Responsible for Size-Dependent Photoluminescence of Colloidal CuInS2 Quantum Dots. *J. Mater. Chem. C* **2014**, *2*, 6867−6872.

https://doi.org/10.1021/acsnano.2c05130
ACS Nano 2022, 16, 12866−12877